

# Fast aerial image simulations for partially coherent systems by transmission cross coefficient decomposition with analytical kernels

Peng Gong

Wuhan National Laboratory for Optoelectronics, Huazhong University of Science and Technology,  
Wuhan 430074, China

Shiyuan Liu,<sup>a)</sup> Wen Lv, and Xinjiang Zhou

State Key Laboratory of Digital Manufacturing Equipment and Technology, Huazhong University of Science and Technology, Wuhan 430074, China

(Received 17 August 2012; accepted 30 October 2012; published 26 November 2012)

Aerial image simulation is one of the most critical components in the model-based optical proximity correction (OPC), which has become a necessary part of resolution enhancement techniques used to improve the performance of subwavelength optical lithography. In this paper, a fast aerial image simulation method is proposed for partially coherent systems by decomposing the transmission cross coefficient (TCC) into analytical kernels. The TCC matrix is projected onto a function space whose basis is analytical circle-sampling functions (CSFs) and converted into a much smaller projected matrix. By performing singular value decomposition (SVD) to the projected matrix, its eigenvectors together with the CSFs are used to generate a set of analytical TCC kernels. The proposed method avoids directly performing SVD to the large TCC matrix, making it much more runtime efficient than the conventional SVD method. Furthermore, the grid size of the kernels can be flexibly set to any desired value in aerial image simulations, which is not realizable with the conventional SVD method. The comparison of aerial image intensity errors and edge placement errors calculated by the proposed method and the conventional SVD method has confirmed the validity of the proposed method. An OPC example is also provided to further demonstrate its efficiency. © 2012 American Vacuum Society. [<http://dx.doi.org/10.1116/1.4767442>]

## I. INTRODUCTION

With ever-decreasing feature size, attempts at pushing the limit of optical lithography have made the optical proximity correction (OPC) technique a necessary part of the resolution enhancement techniques used to improve the performance of the lithography process.<sup>1-3</sup> Generally, the model-based OPC process includes both the forward modeling known as lithography simulation and the inverse process, which aims to optimize the mask layout to compensate for and minimize the distortion caused by optical proximity effects. The forward model is repeated a number of times in the inverse optimization algorithm. Therefore, fast aerial image simulation is highly desirable as one of the most critical components in the forward modeling simulations.

The formulation behind the optical imaging process for a partially coherent system can be roughly categorized into the Abbe's theory<sup>4</sup> and the Hopkins' theory.<sup>4-6</sup> Abbe's imaging formulation considers the source as constructed by a number of incoherent source points, and the total aerial image intensity is calculated as the superposition of all the aerial image intensity distributions produced by these source points. Simulation speed based on Abbe's theory is limited because the fast Fourier transform (FFT) is needed for the intensity calculation of every source point. Hopkins' imaging theory, which formulates the aerial image in terms of the transmission cross coefficient (TCC), has been extensively used in fast aerial image simulation. For aerial image simulation based on

Hopkins' theory, the calculation of the four-dimensional (4D) TCC matrix and the four-fold integration is a most time-consuming step. There are various methods introduced to simplify the aerial image simulation, such as the analytical method,<sup>7-9</sup> the pupil shift matrix method,<sup>10,11</sup> and the cross triple correlation method.<sup>12-14</sup> The sum of coherent systems (SOCS) method,<sup>15,16</sup> or the optimal coherent approximation,<sup>17</sup> which approximates the partially coherent system by the superposition of coherent systems, has been introduced and widely used for its capability to avoid the 4D integration, and the simulation speed has thus been dramatically improved. The conventional SOCS algorithm is based on the well-known singular value decomposition (SVD) of a 2D matrix, which is a reformulation of the 4D TCC array by the column stack operation.<sup>15-17</sup> However, the SVD calculation is still time-consuming as the TCC matrix size is usually very large; e.g., when the matrix size is  $720 \times 720$ , the SVD runtime is 6262 s.<sup>18</sup> In addition, the TCC kernels obtained by SVD only have numerical representations. If the aerial image simulation requires to be set at a different resolution (or grid size), the TCC kernels has to be recalculated by performing the time-consuming SVD again to the TCC matrix.

In this paper, we propose a TCC decomposition method that can obtain a set of analytical TCC kernels without directly performing SVD to the large TCC matrix. This is realized by first projecting the TCC matrix onto a circle-sampling function (CSF) space and converting the TCC matrix into a much smaller projected matrix, followed by performing SVD to the projected matrix and generating the analytical TCC kernels with its eigenvectors and the CSFs.

<sup>a)</sup>Electronic mail: shyliu@mail.hust.edu.cn

The main novel concept in this paper is the application of CSFs and circle-sampling theorem in TCC decomposition in polar coordinate to achieve analytical TCC kernels. Generally, TCC can be expressed as an infinite function series with a set of complete and orthogonal basis functions. There are various basis functions that can be used for this purpose, such as Fourier series, Zernike polynomials, and CSFs. Considering that the optical system usually has a high degree of radially symmetry, the CSFs become our first choice in expressing the TCC. Since TCC is always band-limited, we can further apply the circle-sampling theorem to approximate the analytical 4D TCC in polar coordinate as a finite CSF series. Compared to the conventional SVD method, the proposed method has at least two advantages, including the avoidance of directly performing SVD to the large TCC matrix and the expression of TCC kernels in an analytical form. This makes the aerial image simulations not only more runtime efficient, but also more flexible, as SVD is performed to the smaller projected matrix and the grid size of the TCC kernels can be set to any desired value.

The remainder of this paper is organized as follows. Section II introduces the partially coherent imaging principle and the circle-sampling theorem and then describes in detail how to apply the circle-sampling theorem in TCC decomposition and how to obtain the analytical TCC kernels. Section III provides some simulation results to demonstrate the validity and efficiency of the proposed method. Finally, we draw some conclusions in Sec. IV.

## II. THEORY

### A. Partially coherent imaging system

The imaging process in optical lithography can be modeled as a pupil function with a partially coherent illumination source, namely the partially coherent system, as shown in Fig. 1. According to Hopkins' theory,<sup>4-6</sup> the intensity on the image plane in the spatial domain can be expressed as

$$I(x, y) = \iint TCC(x - x_1, y - y_1; x - x_2, y - y_2) \times O(x_1, y_1) O^*(x_2, y_2) dx_1 dx_2 dy_1 dy_2, \quad (1)$$

where  $O(x_1, y_1)$  and  $O^*(x_2, y_2)$  are the mask pattern and its complex conjugate in the spatial domain, respectively. The TCC is introduced as

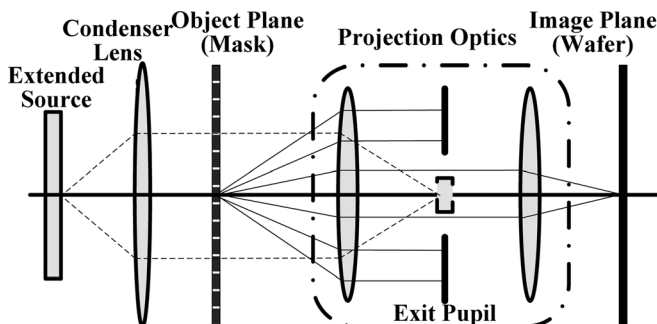


FIG. 1. Partially coherent imaging system used in lithography tools.

$$TCC(x_1, y_1; x_2, y_2) = J(x_1 - x_2, y_1 - y_2) H(x_1, y_1) H^*(x_2, y_2). \quad (2)$$

Here,  $J(x_1 - x_2, y_1 - y_2)$  is the mutual intensity that describes the coherence of the illumination source,  $H(x_1, y_1)$  is the point spread function that fully describes the property of the projection lens, and  $H^*(x_2, y_2)$  is its conjugate.

The TCC is Hermitian and positive definite and can be decomposed into a set of eigenvalues with corresponding eigenvectors. In the numerical simulation, the TCC can be sampled and represented as a discrete 4D array with  $M \times M \times M \times M$  elements, which can be further unfolded into a discrete 2D  $M^2 \times M^2$  matrix  $\mathbf{T}$  by the column stack operation  $\eta$ . The SVD algorithm can be applied to the discrete 2D matrix  $\mathbf{T}$ , yielding the decomposition<sup>15-17</sup>

$$\mathbf{T} = \sum_{k=1}^{M^2} \lambda_k \mathbf{u}_k \mathbf{u}_k^H, \quad (3)$$

where  $\lambda_k$  is the  $k$ th eigenvalue of  $\mathbf{T}$ ,  $\mathbf{u}_k$  is the corresponding  $M^2 \times 1$  eigenvector, and  $\mathbf{u}_k^H$  is its Hermitian conjugate. Applying the inverse column stack operation  $\eta^{-1}$  to  $\mathbf{u}_k$  leads to the 2D  $M \times M$  kernel  $\Psi_k$  of the TCC

$$\Psi_k = \eta^{-1}(\mathbf{u}_k). \quad (4)$$

Thus, the aerial image can be calculated as

$$\mathbf{I} = \sum_{k=1}^{M^2} \lambda_k |\Psi_k \otimes \mathbf{O}|^2. \quad (5)$$

Here,  $\mathbf{O}$  is the discrete matrix that represents the mask pattern  $O(x, y)$ . Usually, only the first several kernels corresponding to the largest eigenvalues are retained to give an approximation of the aerial image. The above procedure describes how the conventional SOCS method works.<sup>15-17</sup> This method may be highly time-consuming as  $M$  increases and the SVD process takes a long time; furthermore, the kernels obtained by this method only have numerical representations. Here we propose a TCC decomposition method that avoids the SVD process of the large matrix  $\mathbf{T}$  and can obtain analytical TCC kernels based on the circle-sampling theorem.<sup>19-21</sup>

### B. Circle-sampling theorem

If the spatial frequency component of a function  $f(\rho, \theta)$  is band-limited within a circle of radius  $\alpha$ , it can be expressed as an infinite circle-sampling function (CSF) series<sup>19-21</sup>

$$f(\rho, \theta) = \sum_{n=-\infty}^{+\infty} \sum_{s=1}^{+\infty} c_{n,s} \varphi_{n,s}(\alpha\rho, \theta), \quad (6)$$

where  $(\rho, \theta)$  is the polar coordinate, and  $c_{n,s}$  are the expansion coefficients

$$c_{n,s} = \int_0^{+\infty} \int_0^{2\pi} f(\rho, \theta) \varphi_{n,s}(\alpha\rho, \theta) \rho d\rho d\theta. \quad (7)$$

The CSFs are defined as

$$\varphi_{n,s}(\alpha\rho, \theta) = R_{n,s}(\alpha\rho)\exp(jn\theta). \quad (8)$$

Here,  $j = \sqrt{-1}$ ,  $n$  is called the angle factor,  $s$  is the radial factor, and  $R_{n,s}(\alpha\rho)$  is the radial function. There are many types of radial functions can be used for circle sampling, and here we select a Bessel function based formula as

$$R_{n,s}(\alpha\rho) = \frac{4z_{n,s}}{J_{n-1}(\alpha\rho) - J_{n+1}(\alpha\rho)} \frac{J_n(\alpha\rho)}{(\alpha\rho)^2 - z_{n,s}^2}, \quad (9)$$

where  $J_n$  is the  $n$ th order Bessel function of the first kind, and  $z_{n,s}$  is the  $s$ th zero-point of the Bessel function  $J_n$ . Figure 2 depicts some typical radial functions with different angle factor  $n$  and radial factor  $s$ . The radial function is equal to 1 at the corresponding Bessel function's zero-point, and the function values concentrate nearby. The radial functions and the corresponding CSFs satisfy the following orthogonal relation:<sup>19</sup>

$$\int_0^{+\infty} R_{n,s}(\alpha\rho)R_{n',s'}(\alpha\rho)\rho d\rho = 2[\alpha J_{n-1}(z_{n,s}) - \alpha J_{n+1}(z_{n,s})]^{-2}\delta_{s,t}, \quad (10)$$

$$\int_0^{2\pi} \int_0^{+\infty} \varphi_{n,s}(\alpha\rho, \theta)\varphi_{n',s'}^*(\alpha\rho, \theta)\rho d\rho d\theta = 4\pi[\alpha J_{n-1}(z_{n,s}) - \alpha J_{n+1}(z_{n,s})]^{-2}\delta_{s,t}\delta_{m,n}. \quad (11)$$

### C. Aerial image simulation by TCC decomposition with analytical kernels

Supposing that  $\sigma$  is the partial coherence factor of the source in an optical lithography, TCC is always band-limited in  $\pm(1 + \sigma)$ . Noticing that TCC is also Hermitian and positive definite, it thus possible to approximate the analytical 4D TCC in polar coordinate as a finite CSF series

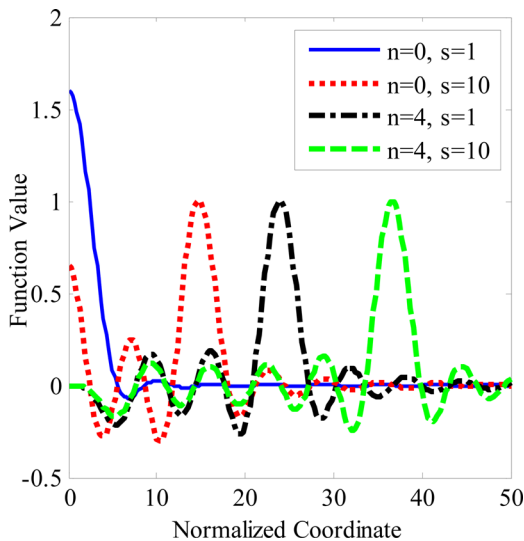


Fig. 2. (Color online) Some typical radial functions with angle factor  $n$  and radial factor  $s$ .

$$TCC(\rho_1, \theta_1; \rho_2, \theta_2) = \sum_{k=1}^N \sum_{l=1}^N p_{k,l} \varphi_k(\alpha\rho_1, \theta_1) \varphi_l^*(\alpha\rho_2, \theta_2), \quad (12)$$

where  $\alpha$  is the maximum spectral content for a radius as introduced in Eq. (8), and it is equal to or larger than  $(1 + \sigma)$  in optical lithography with the partial coherence factor of the source being  $\sigma$ ;  $N = (2N_A + 1)N_R$  is the total number of CSFs with angle factor  $n$  from  $-N_A$  to  $N_A$  and radial factor  $s$  from 1 to  $N_R$ ;  $\varphi_k(\alpha\rho, \theta)$  stands for the  $k$ th CSF; and  $p_{k,l}$  are the expansion coefficients. Note that for simplicity and conciseness, hereafter we denote the CSFs by  $\varphi_k(\alpha\rho, \theta)$  in a one-dimensional (1D) order with only one subscript  $k$ , which is a rearrangement of the CSFs  $\varphi_{n,s}(\alpha\rho, \theta)$  with two subscripts  $n$  and  $s$  as defined in Eq. (8).

In order to obtain the expansion coefficients  $p_{k,l}$ , we first discretize the  $k$ th CSF  $\varphi_k(\alpha\rho, \theta)$  into an  $M \times M$  matrix denoted by  $\Phi_k$ , and then we reformulate  $\Phi_k$  into a discrete 1D vector denoted by  $\mathbf{q}_k$  by using the column stack operation  $\mathbf{q}_k = \eta(\Phi_k)$ . Consequently, Eq. (12) is discretized in a matrix form as

$$\mathbf{T} = \mathbf{Q}\mathbf{P}\mathbf{Q}^H, \quad (13)$$

where  $\mathbf{T}$  is the discrete  $M^2 \times M^2$  TCC matrix, and  $\mathbf{Q}$  is a discrete  $M^2 \times N$  matrix with the  $k$ th column being  $\mathbf{q}_k$

$$\mathbf{Q} = [\mathbf{q}_1 \quad \mathbf{q}_2 \quad \dots \quad \mathbf{q}_N]. \quad (14)$$

The matrix  $\mathbf{P}$  in Eq. (13) is termed the projected matrix with elements  $p_{k,l}$

$$\mathbf{P} = \begin{bmatrix} p_{1,1} & p_{1,2} & \dots & p_{1,N} \\ p_{2,1} & p_{2,2} & \dots & p_{2,N} \\ \dots & \dots & \dots & \dots \\ p_{N,1} & p_{N,1} & \dots & p_{N,N} \end{bmatrix}. \quad (15)$$

Noticing that  $\mathbf{q}_k$  is the discretized form of the  $k$ th CSF  $\varphi_k(\alpha\rho, \theta)$  that has the orthogonal relation shown in Eq. (11), we also have the orthogonal relation for  $\mathbf{q}_k$  as

$$\mathbf{q}_k^H \mathbf{q}_l = \delta_{k,l}. \quad (16)$$

The orthogonal relation in Eq. (16) makes the matrix  $\mathbf{Q}$  in Eq. (14) satisfy

$$\mathbf{Q}^H \mathbf{Q} = \mathbf{I}, \quad (17)$$

where  $\mathbf{I}$  is an  $N \times N$  unit matrix. As a result, the projected matrix  $\mathbf{P}$  can be calculated as

$$\mathbf{P} = (\mathbf{Q}^H \mathbf{Q}) \mathbf{P} (\mathbf{Q}^H \mathbf{Q}) = \mathbf{Q}^H (\mathbf{Q} \mathbf{P} \mathbf{Q}^H) \mathbf{Q} = \mathbf{Q}^H \mathbf{T} \mathbf{Q}. \quad (18)$$

The projected matrix  $\mathbf{P}$  is also Hermitian and positive definite, so we can perform SVD to further decompose it into eigenvalues and eigenvectors, as

$$\mathbf{P} = \sum_{k=1}^N \mu_k \mathbf{v}_k \mathbf{v}_k^H, \quad (19)$$

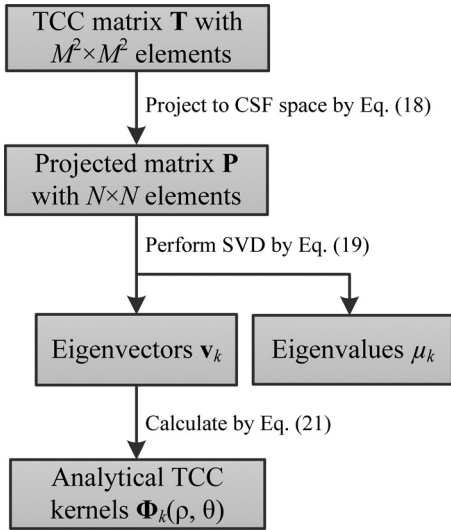


FIG. 3. Flowchart of TCC decomposition into analytical kernels.

where  $\mu_k$  is the  $k$ th eigenvalue and  $\mathbf{v}_k$  is the corresponding eigenvector. Substituting Eq. (19) into Eq. (12), we can analytically calculate the 4D TCC as

$$TCC(\rho_1, \theta_1; \rho_2, \theta_2) = \sum_{k=1}^N \mu_k \Phi_k(\alpha\rho_1, \theta_1) \Phi_k^*(\alpha\rho_2, \theta_2). \quad (20)$$

Here, we call  $\Phi_k(\rho, \theta)$  the  $k$ th analytical TCC kernel, which can be calculated as

$$\Phi_k(\rho, \theta) = \sum_{l=1}^N v_{k,l} \varphi_l(\alpha\rho, \theta), \quad (21)$$

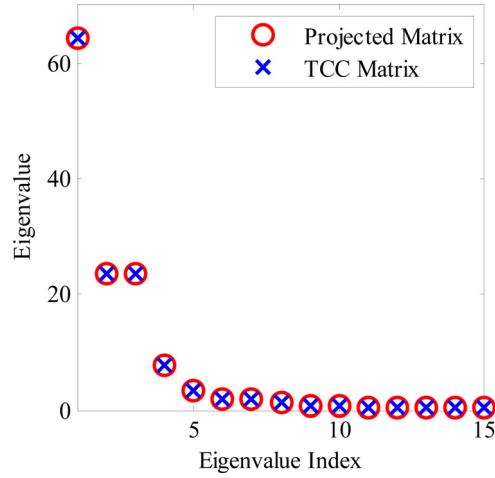


FIG. 4. (Color online) First 15 eigenvalues of the projected matrix and the TCC matrix.

where  $v_{k,l}$  is the  $l$ th element of  $\mathbf{v}_k$ . Instead of Eq. (5), the aerial image can be calculated as

$$\mathbf{I} = \sum_{k=1}^N \mu_k |\Phi_k \otimes \mathbf{O}|^2. \quad (22)$$

The flowchart of TCC decomposition into analytical kernels is shown in Fig. 3. It is noted from Eq. (18) that the projected matrix  $\mathbf{P}$  is the representation of the TCC matrix on the CSF space, so the first several eigenvalues of the projected matrix and the TCC matrix that have higher dominance, should be the same. At the same time, eigenvalues that have lower dominance do not have to be the same because of the residual errors. The kernels obtained by the proposed method and

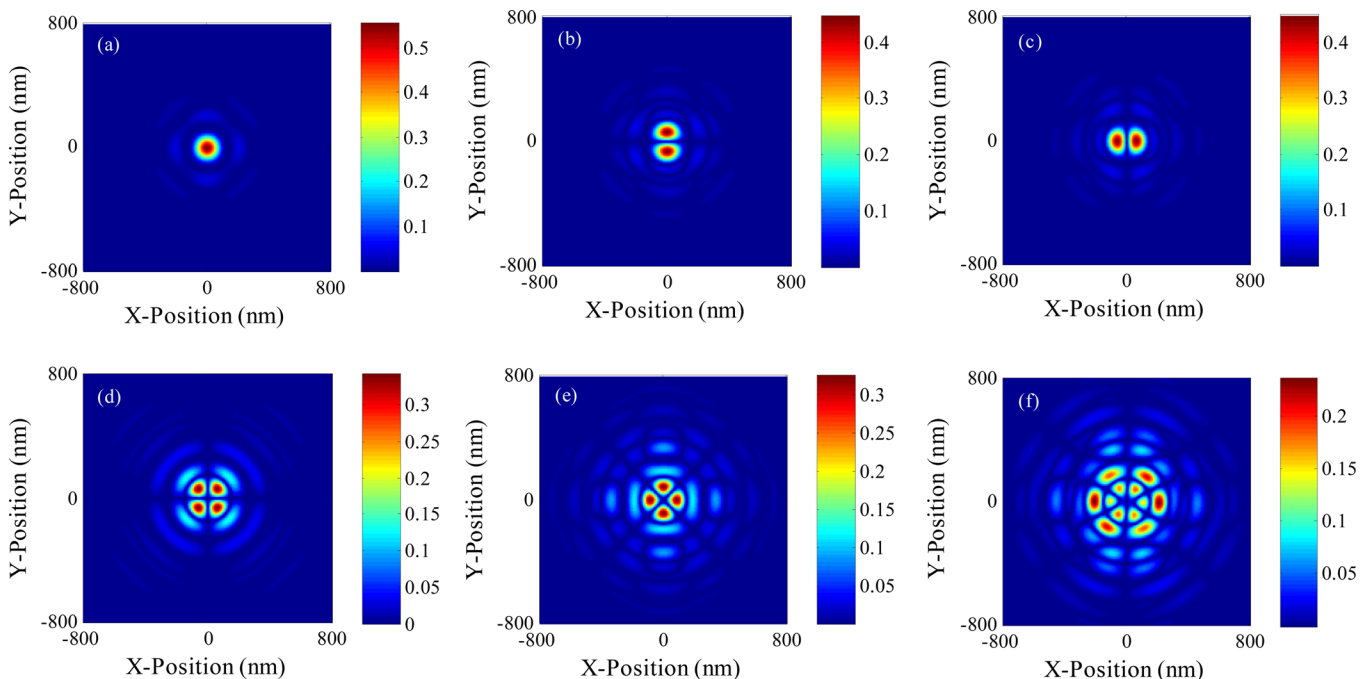


FIG. 5. (Color online) First six kernels derived by the proposed method. (a)–(f) denote the kernels  $\Phi_1(\rho, \theta)$  to  $\Phi_6(\rho, \theta)$ , respectively.

the conventional method do not have to be the same because the TCC matrix has degenerate eigenvalues, and the kernels corresponding to the degenerate eigenvalues can be linearly combined to produce new kernels.

It is particularly worthwhile to point out that the TCC kernels have analytical forms as shown in Eq. (21), so we can set the grid size of the kernels to any desired value directly in aerial image simulation. This merit is not realizable in the conventional method, which directly performs SVD to the 2D matrix  $\mathbf{T}$  and obtains numerical kernels.

### III. SIMULATIONS

We performed simulations on a partially coherent system for a quadrupole illumination source with  $\sigma_{\text{out}} = 0.85$ ,  $\sigma_{\text{in}} = 0.65$ , and degree =  $45^\circ$ . The wavelength in the simulation was set to 193 nm, and the numerical aperture was set to 0.85. The discrete TCC matrix  $\mathbf{T}$  is a  $51^2 \times 51^2$  matrix. A total of 170 CSFs with angle factor  $n$  from  $-8$  to  $8$  and radial factor  $s$  from 1 to 10 were used to form the function space, and the parameter  $\alpha$  of the CSFs as introduced in Eq. (8) was set to 12. Consequently, the projected matrix  $\mathbf{P}$  is a  $170 \times 170$  matrix, which is much smaller than the discrete TCC matrix  $\mathbf{T}$ . In the simulations, the grid size of the kernels and the aerial image were both set to 1 nm, and the ambit of the kernels was set to 800 nm, resulting in 801 points in each axis direction. All of the simulations were performed on a Workstation of 2.54 GHz Opteron with MATLAB in Windows 7 (64-bit).

Figure 4 shows the first 15 eigenvalues of the projected matrix and the TCC matrix. The first 10 eigenvalues of the projected matrix fit very well with those of the TCC matrix, as expected, while the rest of the eigenvalues that have lower dominance are different because of residual errors and the different calculation methods. The difference between the lower dominance eigenvalues does not matter because we only use the first six kernels of higher dominance to calculate the aerial image. Figure 5 depicts the first six spatial domain kernels obtained by the proposed method. Here, because the kernels have analytical forms, we directly set the grid size of the kernels to 1 nm to obtain a  $1601 \times 1601$  matrix. For the conventional method, it is not very realistic to directly obtain a  $1601 \times 1601$  kernel, because the time for performing SVD on a  $1601^2 \times 1601^2$  matrix would be very excessive. In fact, as the discrete TCC matrix  $\mathbf{T}$  we used was a  $51^2 \times 51^2$  matrix, we only obtained a  $51 \times 51$  kernel by the conventional SVD method, which cost 123.1 s for the calculation. In contrast, the runtime for obtaining the  $1601 \times 1601$  kernel was only 3.27 s by using the proposed method. It thus has demonstrated that the proposed method has a much higher speed than the conventional method, as it avoids directly performing SVD to the large TCC matrix.

We did not compare the kernels obtained by the proposed method and the conventional method, because the kernels do not have to be the same. Instead, aerial image simulations were carried out to evaluate the accuracy of the proposed method. We calculated the aerial image of a five bar pattern and a contact cross pattern to confirm the validity of the

proposed method. The mask pattern region is  $[-600 \text{ nm}, 600 \text{ nm}]$  in both axis directions. For the five bar pattern, the width of all the bars is 90 nm. For the contact cross pattern, the width of the central contact is 300 nm, and the width of all the surrounding contacts is 200 nm. The optical parameters in this simulation were the same as in the previous simulation for the calculation of TCC kernels. The normalized mean square error was used to evaluate the difference between the aerial image intensity obtained by the proposed method and that by the conventional SVD method

$$e(\mathbf{A}, \mathbf{B}) = \frac{\sum_{i=1}^m \sum_{j=1}^n |a_{ij} - b_{ij}|^2}{\sum_{i=1}^m \sum_{j=1}^n |a_{ij}|^2}, \quad (23)$$

where  $\mathbf{A} = [a_{ij}]$  and  $\mathbf{B} = [b_{ij}]$  denote the two matrices that represent the aerial image intensity calculated by the proposed method and by the conventional method respectively.

As shown in Fig. 6, the contours of the aerial image obtained by the proposed method fit very well with those

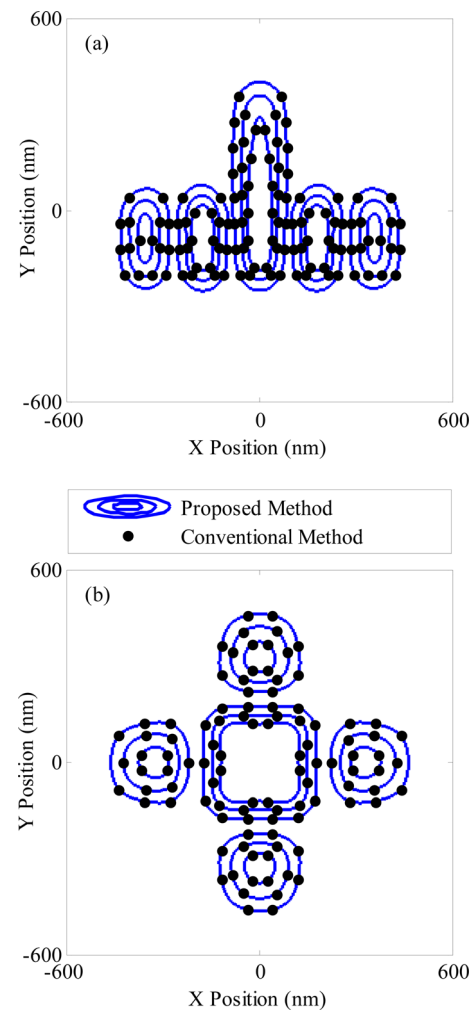


Fig. 6. (Color online) Simulation result of the aerial image contours by the proposed method and the conventional SVD method for (a) a five bar pattern and (b) a contact cross pattern.

provided by the conventional method. The differences between the aerial images, which are normalized by the largest intensity, are also shown in Fig. 7. The normalized mean square error is 0.0023% for the five bar pattern, and 0.00059% for the contact cross pattern. All the simulation results demonstrate that the aerial images calculated by the proposed method have a high accuracy compared to those obtained by the conventional method, which confirms the validity of the proposed method.

Edge placement error (EPE) has been popularly used in OPC, especially in the polygon-based OPC, to convey critical dimension (CD) information, which is essentially the CD error at one side.<sup>16</sup> Generally, for evaluating OPC optimization result, the mean EPE is introduced and defined as a weighted average EPE of all segments as

$$\overline{EPE} = \frac{\sum_{i=1}^S \omega_i |EPE_i|}{\sum_{i=1}^S \omega_i}, \quad (24)$$

where  $EPE_i$  refers to the EPE of the  $i$ th segment,  $S$  is the total number of segments, and  $\omega_i$  is the weighted fact and is set to 1 in all of our simulations.

Figure 8(a) depicts the EPEs obtained by the proposed method and the conventional method for a more complicated

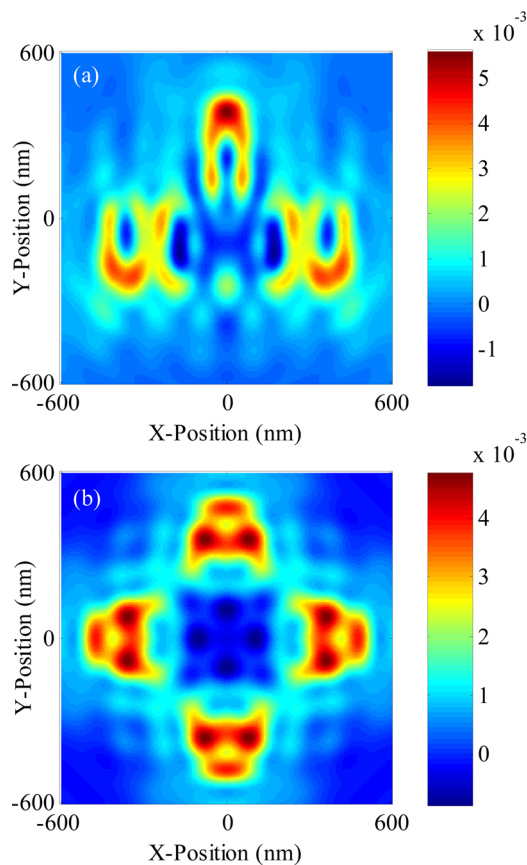


Fig. 7. (Color online) Difference between aerial images obtained by the proposed method and the conventional SVD method for (a) a five bar pattern and (b) a contact cross pattern.

pattern as shown in Fig. 8(b). The pattern region was  $[-1000 \text{ nm}, 1000 \text{ nm}]$  in both directions, and totally up to 57 cutlines at various locations of the pattern were analyzed, as marked by the red lines in Fig. 8(b). Without losing generality, a constant threshold resist (CTR) model was simply introduced to generate the output pattern of the resist image.<sup>22</sup> Other parameters in this simulation were the same as in the previous simulation for the comparison of aerial image intensity error. It is noted from Fig. 8(a) that almost all the EPEs are identical by the proposed method and the conventional method. Actually, the mean EPE obtained by the proposed method is 17.21 nm as compared to 17.16 nm by the conventional method. This means that the calculated CD error is as small as 0.04625% between the two methods, which indicates that the accuracy of the proposed method is highly acceptable.

To further demonstrate the efficiency of the proposed method, we applied it in OPC optimization for the complicated pattern as shown in Fig. 8(b). We adopted a simplified OPC optimization flow reported in our previous work<sup>23</sup> but

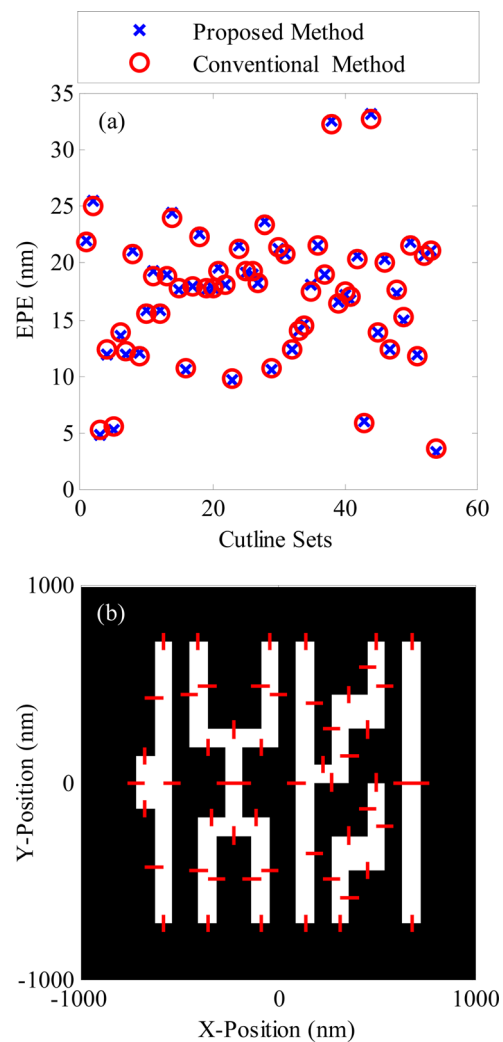


Fig. 8. (Color online) (a) Simulation result of EPEs obtained by the proposed method and the conventional SVD method for (b) a more complicated pattern with red lines indicating the locations of cutlines.

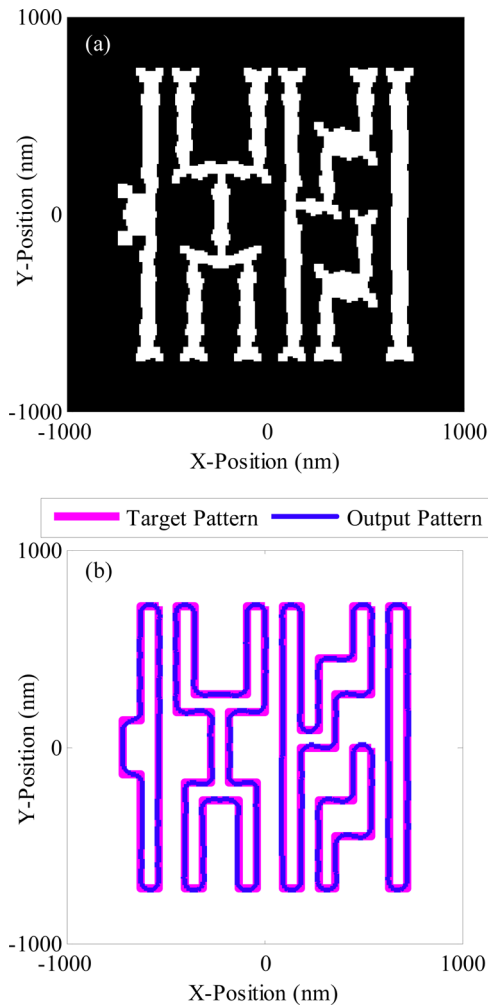


Fig. 9. (Color online) Simulation result of OPC optimization by applying the proposed method with (a) the optimized mask pattern and (b) the contours of the target pattern and the output pattern.

with the forward aerial image simulation performed by the proposed method in this paper. The fragmentation lengths along the lines and near the corners were set to of 30 nm and 10 nm respectively, and the mean EPE for all segments was used as a cost function for evaluating the optimization effect. Other parameters in this simulation were the same as in the previous simulation for the comparison of EPEs, including using the CTR model to generate the output pattern of the resist image.<sup>22</sup>

The optimized mask pattern after eight iterations is depicted in Fig. 9(a), and the contours of the target pattern and its corresponding output pattern of the resist image are shown in different line types in Fig. 9(b). It is observed that the output pattern has a high fidelity with the target pattern; thus, the proposed approach is expected to be applicable in OPC systems. Actually, the mean EPEs of the output pattern before and after the OPC process are 18.35 nm and 3.54 nm, respectively, indicating that the optimized mask pattern has dramatically reduced the CD errors of the output pattern. Furthermore, the total runtime for the whole OPC process is 28.2 s, which further demonstrates that the proposed method is fast enough to be applied in OPC systems.

## IV. CONCLUSIONS

We have proposed a fast aerial image simulation method for partially coherent illumination systems based on TCC decomposition with analytical kernels. The large TCC matrix is projected onto the CSF space and converted into a much smaller projected matrix, which is then performed SVD to generate the analytical TCC kernels with its eigenvectors and the CSFs. It has demonstrated that the proposed method avoids directly performing SVD to the large TCC matrix; thus, it is much more runtime efficient than the conventional method. In addition, the TCC kernels derived by the proposed method have analytical forms; thus, the grid size of the kernels can be set to any desired value, which is not realizable with the conventional method. The simulation results by evaluating aerial image intensity errors and mean EPEs have validated the high accuracy of the proposed method, and the provided OPC example has further confirmed its efficiency in OPC applications. For future work, we will extend the proposed method in the hyper NA application by addressing vectorial formulations as well as mask patterns and dimensions that are more computational demanding.

## ACKNOWLEDGMENTS

This work was funded by the National Natural Science Foundation of China (Grant Nos. 91023032, 51005091, and 51121002), the National Science and Technology Major Project of China (Grant No. 2012ZX02701001), and the National Instrument Development Specific Project of China (Grant No. 2011YQ160002).

- <sup>1</sup>A. K. K. Wang, *Resolution Enhancement Techniques in Optical Lithography* (SPIE Press, Bellingham, WA, 2001).
- <sup>2</sup>N. Cobb and A. Zakhor, *Proc. SPIE* **2440**, 313 (1995).
- <sup>3</sup>A. Poonawala and P. Milanfar, *IEEE Trans. Image Process.* **16**, 774 (2007).
- <sup>4</sup>A. K. K. Wang, *Optical Imaging in Projection Microlithography* (SPIE Press, Bellingham, WA, 2005).
- <sup>5</sup>H. H. Hopkins, *Proc. R. Soc. London, Ser. A* **217**, 408 (1953).
- <sup>6</sup>M. Born and E. Wolf, *Principles of Optics*, 7th ed. (Pergamon, Oxford, 1999).
- <sup>7</sup>E. Kintner, *Appl. Opt.* **17**, 2747 (1978).
- <sup>8</sup>R. L. Gordon, *Proc. SPIE* **4692**, 517 (2002).
- <sup>9</sup>R. L. Gordon and A. E. Rosenbluth, *Proc. SPIE* **5182**, 73 (2004).
- <sup>10</sup>K. Yamazoe, *J. Opt. Soc. Am. A* **25**, 3111 (2008).
- <sup>11</sup>K. Yamazoe, *J. Opt. Soc. Am. A* **27**, 1311 (2010).
- <sup>12</sup>S. Y. Liu, W. Liu, and T. T. Zhou, *J. Mirco/Nanolith. MEMS MOEMS* **10**, 023007 (2011).
- <sup>13</sup>S. Y. Liu, W. Liu, and X. F. Wu, *Chin. Phys. Lett.* **28**, 104212 (2011).
- <sup>14</sup>S. Y. Liu, S. Xu, X. F. Wu, and W. Liu, *Opt. Express* **20**, 14221 (2012).
- <sup>15</sup>N. Cobb and A. Zakhor, *Proc. SPIE* **2621**, 534 (1995).
- <sup>16</sup>N. Cobb, "Fast optical and process proximity correction algorithms for integrated circuit manufacturing," Ph.D. dissertation (University of California at Berkeley, 1998).
- <sup>17</sup>Y. Pati and T. Kailath, *J. Opt. Soc. Am. A* **11**, 2438 (1994).
- <sup>18</sup>R. Sabatier, C. Fossati, S. Bourennane, and A. D. Giacomo, *Opt. Express* **16**, 15249 (2008).
- <sup>19</sup>H. Gamo, "Matrix treatment of partial coherence," in *Progress in Optics*, edited by E. Wolf (North-Holland, Amsterdam, 1964), pp. 187–332.
- <sup>20</sup>H. Stark, *J. Opt. Soc. Am.* **69**, 1519 (1979).
- <sup>21</sup>N. E. Myrdis and C. Chamzas, *IEEE Trans. Med. Imaging* **17**, 294 (1998).
- <sup>22</sup>W. Huang, C. Lin, C. Kuo, C. Huang, J. Lin, J. Chen, R. Liu, Y. Ku, and B. Lin, *Proc. SPIE* **5377**, 1536 (2001).
- <sup>23</sup>S. Y. Liu, X. F. Wu, W. Liu, and C. W. Zhang, *J. Vac. Sci. Technol. B* **29**, 06FH03 (2011).